This is a repository copy of *A two-dimensional organic-exciton polariton lattice fabricated using laser patterning*.

Article:

A two-dimensional organic-exciton polariton lattice fabricated using laser patterning

Rahul Jayaprakash[1], Charles E. Whittaker[1], Kyriacos Georgiou[1], Onkar Game[1], Kirsty E. McGhee[1], David M. Coles[1,†], and David G. Lidzey[1,*]

[1]Department of Physics and Astronomy, The University of Sheffield, Hicks Building, Hounsfield Road, Sheffield S3 7RH, United Kingdom.

ABSTRACT: Exciton-polaritons in 2D lattice geometries now attract considerable attention as systems in which to explore new physics. However, such structures are relatively difficult to fabricate as this can involve sophisticated milling or etching of cavity layers to create arrays of defects. Here, a straightforward technique is reported that allows rapid fabrication of 2D polariton lattices that operate at room temperature. Specifically, laser patterning has been used to write a 2D square lattice of defects into a sacrificial polymer layer. An organic microcavity structure is then built on top of the patterned polymer, with the morphology of the patterned polymer propagating through the subsequent layers and spatially modifying the optical path-length of the active cavity region. Using real- and momentum-space spectroscopy, the formation of gapped polaritonic band structures has been demonstrated at room temperature. The optical writing approach discussed here opens up the way for fabrication of more complex 2D-lattice geometries for studying topological physics at room temperature.

By engineering a periodic lattice of pillars or holes into a two-dimensional (2D) dielectric medium, it is possible to engineer an optical lattice that is in many cases analogous to the electronic band-structures typical of inorganic crystalline semiconductors. Such structures allow exotic states to be explored, including Dirac cones [1], flat bands[2] or edge states[3] that are associated with novel transport and localization phenomena. Indeed, such ideas have already been applied in a diverse range of material systems, including silicon ring resonator arrays[4,5], coupled optical waveguides[6,7], microwave resonator arrays[8,9] and metamaterials[10]. Such lattices can be defined by physical lithography techniques [10.1038/s41586-018-0601-5] or instead patterned using lithography-free techniques (e.g. using a spatial light modulation technique) with the distance between states engineered dynamically [10.1038/nmat4971]. Importantly, the measurement of optical emission from 2D optical lattices offers direct optical access to the amplitude, phase and coherence properties of the states that are supported. Significantly, optical lattice structures can be used as media in which to simulate complex phenomena and explore fundamental effects relating to disorder, strain, spin-orbit coupling and topological order.

Exciton-polaritons are hybrid quasiparticles formed by strongly coupling a confined optical mode within a microcavity to the electronic excitations of a semiconductor.

Here, the mixed light-matter character of polaritons combines a small effective mass inherited from their photonic component along with pronounced non-linearity originating from their excitonic component. This unique combination of properties, together with their bosonic nature permits macroscopic quantum phenomena to be explored, including polariton-condensation[11], superfluidity[12] and the formation of solitons[13,14]. Exciton-polaritons can also be sensitive to magnetic fields; a property that facilitates the realization of injection lasers[15] and other devices[16]. Strongly-coupled microcavities are now attracting attention as systems in which to implement 2D lattice structures[17–19], as such structures can support topologically protected transport[20], with the condensation of polaritons potentially allowing the simulation of complex many body Hamiltonians[21] including the classical XY hamiltonian [10.1038/nmat4971]. Indeed, by characterizing photoluminescence (PL) in either real or momentum space it is possible to directly determine lattice band-structure and image the propagation of polariton wave packets along the edge of the so-called honeycomb lattice[19].

Photonic lattices defined into inorganic semiconductor microcavites therefore show great potential for both technological applications and as a testbed for exploring fundamental physics. However, the low binding energy typical of III-V inorganic semiconductor excitons limits the
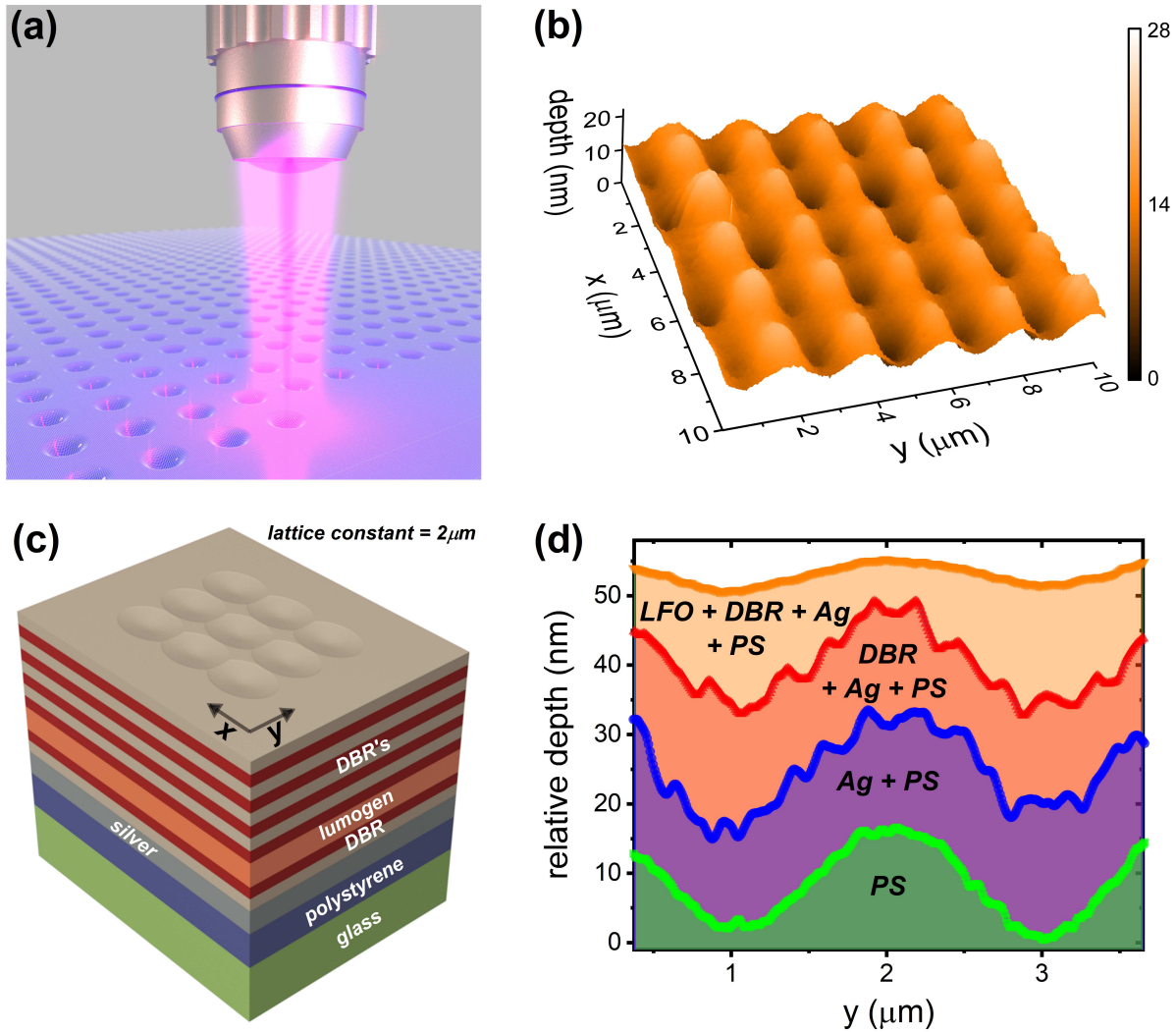
Figure 1. Part (a) Shows a schematic of the use of a focused laser beam to pattern an array of defects into a PS layer. Part (b) is an SFM scan of the surface of a patterned PS film. An array of Gaussian-shaped defects is clearly evident. Part (c) is a schematic of the complete cavity. Here, the structure is fabricated on top of the patterned PS film. Part (d) shows cross-sections recorded from SFM images taken at various stages in the construction of the microcavity. The image demonstrates that the corrugations in the PS layer propagate through the bottom mirror and into the active layer, however the active layer partially planarizes this structure.

observe the relative small Rabi-splittings that occur when using low oscillator strength Mott-Wannier excitons require sophisticated fabrication procedures[22] to define the necessary in-plane confinement potentials. Such limitations are significant and make the rapid development of room-temperature applications problematic.

In this paper, we describe the fabrication of optical lattices in strongly-coupled microcavities containing an organic semiconductor. Here, the Frenkel excitons supported by such materials have very large binding energies (100s of meV) and thus polaritonic effects including polariton-condensation are accessible at room temperature[23–25]. Recent work has demonstrated the fabrication of one-dimensional (1D) soft-matter based polariton lattices, however the techniques used to fabricate the lattice were technologically demanding and required the use of e-beam lithography[26] and ion beam milling[27]. Coupling between localized organic-exciton

polaritonic states has also been achieved by using e-beam patterning to create a series of Gaussian defects into a Distributed Bragg Reflector (DBR), with this mirror placed in close proximity to a second DBR (coated a conjugated polymer) using a piezoelectric actuator.[28] However the creation of such 'open-cavity' structures requires the use of sophisticated fabrication techniques, with such structures being susceptible to the effects of vibrational noise. Other work on structures based on arrays of metallic nanostructures coated with an organic semiconductor forming plasmon-exciton polaritons has also evidenced polariton condensation at room temperature[29,30]. More generally, periodic arrays can be defined into soft polymeric media using techniques such as nano-imprint lithography[31]. Such embossing techniques can combine high fidelity and precision, with the structures realized being used to create a range of optical devices including distributed feedback organic lasers[32].

Here, we demonstrate the use of a simple, optical printing technique that we use to write a large 2D lattice into a polymer layer, with this structure being transferred to the active region of a strong-coupled organic semiconductor microcavity that is fabricated monolithically on the surface of the patterned polymer. This process allows us to fabricate 2D arrays of traps into a microcavity in a square-lattice geometry, with angle-resolved PL spectroscopy being used to demonstrate a gapped polaritonic band structure at room temperature. Our results present a straightforward and flexible new method to implement lattice potentials in organic polariton microcavities, and pave the way towards the study of more complex 2D lattice geometries in which we anticipate the formation of 1D edge states.

RESULTS AND DISCUSSION

To fabricate lattice structures, we first deposited a 1150 nm thick layer of the polymer polystyrene (PS) onto a quartz coated glass substrate via spin-coating. Light from a Ti:sapphire laser (445 nm at 76 MHz with a pulse width of ~ 150 fs) was then focused onto the polymer into a spot having a diameter of around 2.5 μm, although this spot was in fact slightly elliptical as discussed below (see Figure 1(a)). The incident laser light was partially absorbed by the PS and caused sufficient heating to initiate local melting. The expansion associated with this melting caused an outflow and wetting of the surrounding polymer - a process that was possibly accompanied by partial ablation[33]. After the laser was switched off (typically after 2.2 seconds), a slight depression was written into the surface of the PS film. Henceforth, we refer to these features as 'defects', which typically have a Gaussian profile and are surrounded by a rim resulting from the outflow of the melted material. Similar processes have previously been used to pattern polymer films[33–37], although we believe that this is the first time that low energy femtosecond pulses at a repetition rate of 76 MHz have been used for micro-fabrication, although such effects have been predicted using a heat accumulation model.[37]

Using an *XY* translation stage and a shutter to control patterning time, we have written arrays of defects having an average depth of 16 nm into a PS film, where the patterning time per defect point was around 1.5 seconds. Figure 1(b) shows a scanning force microscopy (SFM) image of part of a patterned lattice. Here a (22 x 18) μm square lattice array composed of 120 defects was patterned, with the lattice having a lattice constant of 2 μm. Indeed, by controlling writing conditions, we have been able to reduce the lattice constant to 1.8 μm, with further reductions expected through the use of a higher NA objective lens and a shorter-wavelength patterning laser. We have also created isolated defects and pairs of defects that allow us to explore confinement effects in a single defect and the tunneling of polaritons between neighboring defects. Following extensive optimization, we have found that the depth of the defects can be controlled by adjusting the laser power density and the exposure time used to write each defect, with defects having depths between 5 and 22 nm realized through control of writing conditions. Indeed, we have found that the depth of the defects can be increased even further if desired by both adjusting the writing conditions and by using thicker polystyrene layers. Our control over the patterning process is relatively good, and we find that the average value of the

depth of 15 defects patterned into an array varied by no more than ± 10% of their average value.

Note that use of a laser patterning technique has the advantage compared to conventional imprint lithography, that lattice design can be rapidly modified without the need to produce a new mold. Furthermore, we emphasize that although our lithography is currently performed using a serial process, we believe that it could be easily parallelized using a spatial light modulator (SLM) to break the incident writing beam into an array of independent laser beams. This process may well allow additional control of the depth and shape of the defects, as well as allowing the lattice pattern to be rapidly modified by programming the SLM. Indeed, we expect much larger lattice arrays could be written by stitching smaller arrays together.

Figure 1(b) indicates that the Gaussian defects created have slightly different barrier heights and widths along the x and y directions. Our analysis of the image indicates that the average barrier height along the x direction being around 50% of that along the y direction, with the average width of the defect being > (1.2 ± 0.1) and (0.9 ± 0.1) μm along the x and y directions respectively (see Supplementary Information (SI) for further details). This small asymmetry indicates that the defects are slightly elliptical; a result that we believe stems from an ellipticity in the patterning laser-beam. Note that the width of the defects can be controlled to some extent by either adjusting the writing time (longer writing times generally lead to narrower defects) or via control of the lattice constant which affects the relative overlap between defects and thereby impacts on their linewidth. We believe it may well be possible to reduce the linewidth of the patterned defects through control of laser pattering wavelength and by increasing the numerical aperture of the objective (patterning) lens.

A strongly coupled microcavity was then fabricated onto a patterned PS surface, as shown schematically in Figure 1(c). This structure was constructed by first depositing a 200 nm silver mirror on top of the patterned PS, with this mirror then coated by a single $\lambda/4$ thick SiO_2 / Nb_2O_5 DBR pair. This 'hybrid' mirror (composed of a metallic film and a metal-DBR), combines both high reflectivity (around 98.6% at λ = 619.6 nm) and ease of construction. This mirror was then covered by the cavity active layer, which consisted of a layer of the fluorescent molecular dye Lumogen F Orange (LFO) dispersed into a PS matrix, with this film deposited by spin-coating. Finally, the structure was completed by depositing a top DBR consisting of 8 pairs of Nb_2O_5 / SiO_2. A detailed description of all fabrication steps can be found under Materials and Methods. As we show below, the defects written into the polystyrene layer are transferred to the active region of the organic semiconductor microcavity that is fabricated onto its surface. Note that patterning a layer placed beneath the cavity confers two significant advantages compared with a process in which the active layer is directly patterned[38]. (1) The patterning process is decoupled from processing the active layer; indeed, it should be possible to create defects in the cavity region whose depth is significantly larger than that of the active layer film. (2) Our process avoids exposing the active organic layer to the patterning laser. This approach is different from other work in which the active layer is directly patterned to locally

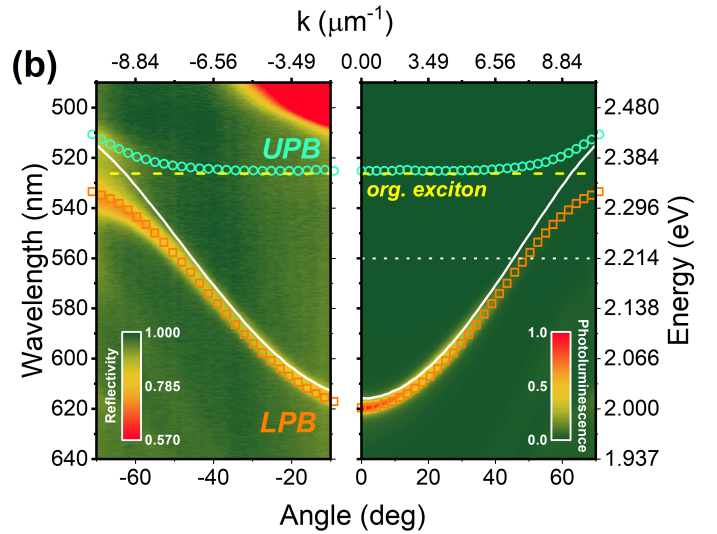change its refractive index[38], and thereby avoids photo-oxidation or photo-bleaching of the active layer.
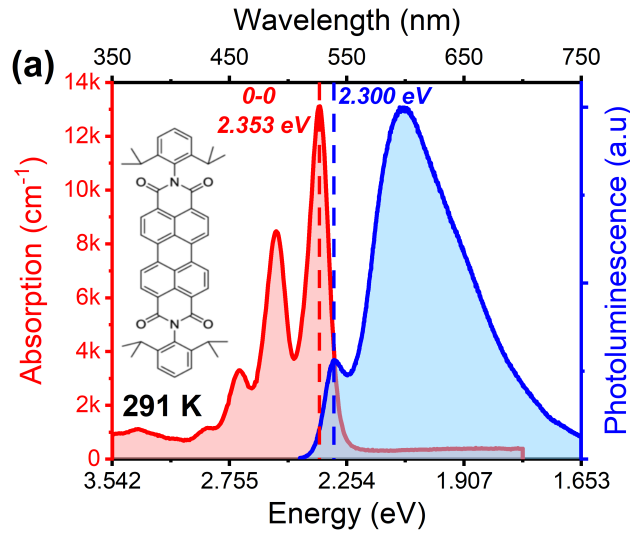
Figure 2. Part (a) shows the absorption and PL of the molecular dye LFO when dispersed into a PS matrix. The chemical structure of LFO is shown as an inset. Part (b) (left-hand panel) shows the white-light angle dependent reflectivity of an un-patterned region of the cavity. The corresponding PL emission from an un-patterned cavity region is shown in the right hand panel.

is shown in Figure 1(d), where we plot topography cross-sections recorded at various stages of the structure fabrication. Here, it can be seen that a significant modulation in surface topography of the patterned PS layer (shown by the green shaded area), with the defects having an apparent depth of around 16 nm. These defects are still detectable after the deposition of the silver layer (blue shaded area) and after the deposition of the bottom DBR (red shaded area). The unchanged relative depth of the defects observed after coating with silver and DBR layers indicates that such materials coat the patterned surface conformally. However, the apparent depth of the defects is reduced to around 5 nm after deposition of the LFO layer (orange shaded area), suggesting that this layer partially planarizes the patterned surface. This planarization process is critical, because – as we show below – it results in elongated regions in the cavity region, that act as an energetic trap for polaritons, with - as we show below - the 2D pattern creating an optical lattice.

In Figure 1(d) it is apparent that the use of the silver layer introduces a degree of roughness into the active layer. We have measured the RMS roughness of the different layers as the cavity is constructed at an un-patterned location away from the patterned region using SFM imaging. We find that the surface of the PS film (green shaded line) has a roughness of ~ 1.9 nm. When coated with a silver film, the roughness of the surface increases to ~ 2.8 nm, with this affect attributed to the grain structure of the silver layer. This roughness then propagates through the structure following the deposition of the one-pair DBR, however after coating this surface with the PS / LFO layer, the surface roughness was reduced to ~ 1.1 nm. We find that the Q-factor of the cavity determined from a region away from the patterned area to be around 500; a value in close accord with the Q-factor predicted using a Transfer Matrix (TM) model (see Materials and Methods) for a nominally identical structure based on ideal layers. It appears therefore that the presence of the slightly roughened silver layer does not appear to significantly impact on the overall Q-factor of the structure.

We have characterized individual steps in the cavity fabrication and deposition process using SFM imaging. This

We note however that the Q-factor of our cavities is still small in comparison with that of 1D organic polariton lattice structures[27] that have reported Q-factors in excess of 20,000. We believe that this difference in Q-factor can however be attributed to a difference in structure design.

We now discuss the organic semiconductor material used as the cavity active layer. Figure 2(a) plots the optical absorption, PL emission and chemical structure of the LFO dye when dispersed in a PS matrix. This material was chosen as the active medium in a strong-coupled cavity due to its relatively narrow 0-0 absorption peak located at 2.353 eV that has a full width half maximum linewidth of 70 meV. It can be seen that there are two other vibrational transitions evident at higher energy. The high absorption coefficient of the 0-0 transition (13,000 cm^{-1}) together with a relatively small Stokes shift of ~ 52 meV makes this dye an ideal material to observe strong coupling. The figure also plots the PL emission from LFO in PS. Here, it can be seen that there is a peak evident at 2.3 eV that corresponds to emission from the 0-0 transition. However, this is significantly weaker than a broad emission peak that is centered around 2.066 eV that we attribute to emission from intermolecular states such as excimers.

We can demonstrate that our structures operate in the strong coupling regime by performing angle dependent reflectivity and PL measurements on un-patterned regions of the sample. Figure 2(b), (left-hand panel) plots white-light cavity reflectivity as a function of external viewing angle. Here, we find the reflectivity is characterized by two branches that we identify as the lower (LPB) and upper (UPB) polariton branches that undergo anti-crossing around the energy of the LFO 0-0 peak. Note that the upper branch feature (present at angles above 60º) is rather weak. Here the detection of this feature is complicated by the strong negative detuning of the cavity which means it mostly lies outside the angular range of our goniometer system (10 - 70º). In the accompanying PL emission data (right-hand panel), we find that emission only occurs from the LPB, with

most of the emission concentrated around $k = 0$ and at energies lower than 2.214 eV (shown using a dashed white line in Figure 2(b)). This emission pattern is consistent with a radiative pumping mechanism in which the radiative decay of weakly coupled excimers in the exciton reservoir 'pumps'

the photon-like component of the polariton states. The efficiency of this process is maximized for photon-like states; a process that qualitatively explains the relatively strong emission from the bottom of the (photon-like) lower polariton branch[39]. The observed Stokes shift of
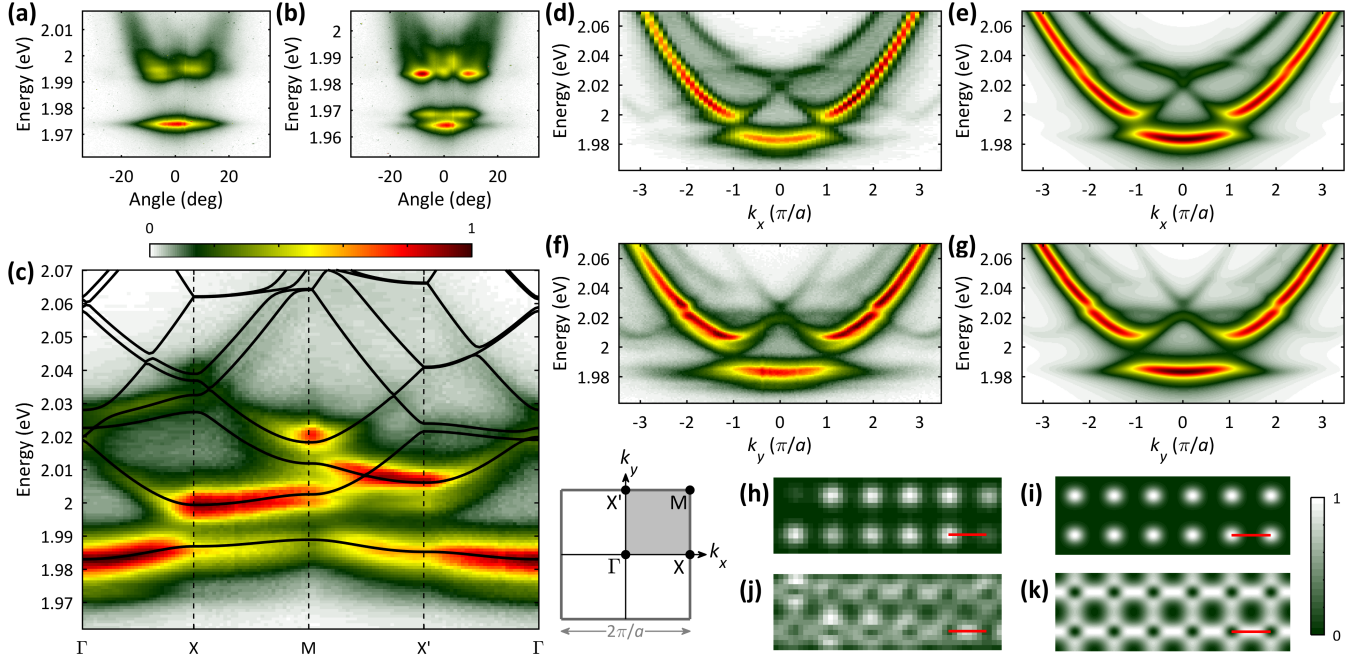

Figure 3. PL measurements from patterned regions of the sample. Angle-resolved PL spectra are shown from single (a) and coupled (b) defects measured along the y direction. (c), Experimental measured band structure from a 2D square lattice plotted along the high symmetry points Γ, X, M and X', together with calculated band structure (solid black lines). Lower right, Schematic of the first Brillouin zone. (d-g), Experimental (d) and calculated (e) dispersion along k_x at $k_y = 0$, and experimental (f) and calculated (g) dispersion along k_y at $k_x = 0$. (h-k), Experimental (h) and calculated (i) real space emission from the s modes, and experimental (j) and calculated (k) real space emission from the p modes. The red scale bars are 2 μm.

emission to lower energies also explains the absence of emission from the UPB.

We can fit reflectivity and PL data using a TM model and overlay our simulations on the color maps shown in Figure 2(b). Here, our best fit indicates a Rabi splitting between the LPB and UPB of ~ 100 meV. Note that we do not detect any energetic crossing between the cavity photon and the first vibronic replica at 2.532 eV. This is because the cavity is so negatively detuned that the cavity photon cannot interact with this state even at very high wave vectors. We have also fitted the quasi-parabolic dispersion of the LPB using a coupled oscillator model in order to extract the effective mass of the polaritons ($1.1 \times 10^{-5} m_e$), with this number used in our simulations of the dispersion of polaritons in a modulated potential as described below.

We now discuss optical characterization measurements made on (i) a single defect, (ii) a pair of defects and (iii) the square lattice arrays that were patterned into a strong-coupled cavity. Here, optical measurements were performed using both Fourier-space and real-space imaging setups in the linear regime, where the excitation density used was sufficiently low (66 fJ / pulse) that blue-shifts resulting from photobleaching [ref – pavlos paper with us] and non-linear effects are not expected (see Materials and Methods). In an isolated single-defect, the local elongation of the cavity along the cavity axis creates an energetic trap having an average depth of ~ 50 meV along the y direction (see SI for

further details). The cavity polaritons thus experience a lateral confinement by the trap potential as well as the vertical confinement provided by the cavity mirrors. In the presence of this three-dimensional confinement, the cavity dispersion is modified, and takes the form of a series of discrete modes. Figure 3(a) plots the measured PL emission dispersion (determined using Fourier imaging) from a single defect. Here, it can be seen that the two lowest-lying states either have single- or double-lobed emission, corresponding to s- and p-type symmetry respectively. Note that the potential traps shown in Figure 3(a) are not sufficiently deep to confine higher order modes, however higher-order modes can be seen when the depth of the confining trap is increased to ~ 100 meV (along the x direction) by using a longer patterning time (see SI Figure S1). A potential depth of ~ 100 meV created using our laser patterning technique is at least twice as deep as the 'deep periodic potentials'[40] (~ 55 meV) employed in conventional inorganic systems, and highlights the ability of our structures to generate new levels of confinement.

We now consider the effect of bringing two defects into close proximity. The measured PL emission dispersion of two defects separated by 2 μm is shown in Figure 3(b). Here, the overlap via evanescent photonic coupling of the confined polariton wave functions in the two defects induces an energy splitting of the discrete modes. This creates bonding and anti-bonding states having an energetic splitting of 4.2 meV. We note that the ability to form energetic traps

between which polaritons can tunnel is a fundamental prerequisite for the engineering of artificial lattice potentials in microcavities.

We now turn our attention to 2D arrays of defects that have been patterned into a square lattice. We note that the profile of the laser used to pattern the defects was slightly elliptical; a feature that reduces the symmetry of the lattice. In a perfectly square lattice, the full band structure can be defined by plotting a line connecting the high symmetry points Γ, X and M. However, to account for the asymmetry of the lattices studied here, it is necessary to plot the band structure along the Γ-X-M-X'-Γ direction in order to fully describe the system. The emission associated with this reduced Brillouin zone is shown in Figure 3(c) along with the definition of Γ, X, X' and M directions. Here, we overlay experimental data (color map) with a calculation of the band-structure for an infinite square lattice of elliptical Gaussian potentials (shown by solid black lines). It can be seen that there is an excellent agreement between experiment and theory, with our results confirming the formation of a gapped and folded band structure arising from the presence of a periodic potential. One feature that is evident in Figure 3(c) is there are different coupling strengths along x and y directions; a conclusion confirmed by the fact that the energy gap determined at the X and X' points is different (12.5 and 20.8 meV respectively). The band-structure of the square lattice was constructed from energy-momentum relations determined along $k_x = 0$ and $k_y = 0$ directions as plotted in Figures 3(d) and 3(f). Again, differences in the dispersion determined in these different directions originate from a slight asymmetry of lattice in the x and y directions.

It is apparent in Figure 3(c) that PL is not emitted with equal intensity from each of the different bands, with some of the bands being relatively 'dark'. To explain this phenomenon, we calculate the emission intensity of the lattice along the $k_x = 0$ and $k_y = 0$ directions using the expected emission probability of each calculated energy eigenstates (see Materials and Methods). This allows us to calculate the theoretical dispersion of PL emission as shown in Figures 3(e) and 3(g). Here it can be seen that the agreement between measurement and theory is excellent and confirms that emission is as expected for a slightly asymmetric 2D square lattice of Gaussian defects.

We have also measured real space emission from the lattice at various photon energies and compare this with our model of band-structure. This is shown in Figures 3(h) and (j) (measured data) and 3(i) and (k) (simulation) for the s and p bands, which correspond to measured photon energies of 1.984 eV and 2.007 eV respectively. Note that the energy of the s- and p-bands in the single defect, double defects and the square lattice are all slightly different, with this effect resulting from slight variations in cavity layer thickness across the surface of the substrate.

In summary, we have fabricated high quality photonic lattices into a strongly-coupled organic-semiconductor microcavity using an optical printing technique. This technique is easy to implement, rapid and in principle permits lattices to be fabricated with high precision over large areas. We have used this technique to fabricate a square lattice and have characterized the emission from a strongly coupled fluorescent dye that was dispersed in the cavity active layer. Using optical tomography measurements,

we have mapped out the optical band-structure and show that this is in excellent agreement with simulations. Real space emission from the cavity demonstrates uniformity of band-structure across areas > 20 μm^2.

Significantly, we expect the ease of processing organic semiconductors together with the flexibility of the patterning technique to allow us to engineer new effects. For example, it is straightforward to fabricate strongly-coupled semiconductor microcavities containing more than one type of organic material. If such materials support near degenerate Frenkel excitons, then optically driven hybridization between the excitons result in the formation of 'hybrid polariton' states that are admixtures of the cavity photon and the different excitonic states. We have already explored such effects in a range of cavities using a variety of materials[42–44], and have demonstrated that such systems permit efficient energy transfer between excitonic states via hybrid polariton modes. It will be interesting to explore how such energy transfer effects can be modified by the fabrication of laterally patterned lattices.

We believe that an extension of our methods to pattern other lattice geometries is straightforward, including honeycomb and Lieb lattices. Here such structures have uni-directional transport along their edges that is unaffected by defects or disorder. We also expect significant opportunities to explore the room-temperature condensation of organic exciton-polaritons in such lattice structures as has been evidenced in conventional planar microcavities[23–25] and lattices containing exciton-plasmon polaritons[29,30]. Here, such systems potentially allow 1D and 2D Hamiltonians to be emulated and thereby offer a route to simulate complex many body problems [21]. Looking further afield, it will be interesting to combine the lithographically patterned lattices explored here with lattices of polariton condensates prepared using dynamic printing techniques [ref lagoudakis and berlof], allowing a further degree of control over condensate flow, propagation and interaction.

MATERIALS AND METHODS

FABRICATION

Organic film: PS having an average molecular weight (Mw) of 192,000 Da was dissolved in dichloromethane (DCM) at a concentration of 25 mg / mL. LFO dye was then added to the PS / DCM solution at a concentration of 13% by mass. This solution was then spin cast onto the bottom hybrid mirror at 1366 rpm, creating a ~ 400 nm thick film, measured using a Bruker DektakXT profilometer.

Polystyrene layer: PS having an average molecular weight (Mw) of 350,000 Da was dissolved in toluene at a concentration of 100 mg / mL. The solution was heated to 70 °C and stirred at 800 rpm for 30 minutes. This solution was spin cast at room temperature onto a quartz coated glass substrate at 3700 rpm, creating a 1150 nm thick film. The thickness of the PS layer was measured using a Bruker DektakXT profilometer.

Laser patterning of the polystyrene layer: The PS / quartz sample was mounted vertically onto motorized linear stages (Newport MFA-CC) in an XY configuration which was driven by a Newport ESP301 2-axis controller. The optical patterning was performed using a frequency doubled Ti:Sapphire (coherent MIRA 900) laser at 445 nm, having a pulse width of ~ 150 fs, a nominal pulse repetition rate of ~ 76 MHz and an average power of ~ 23.5 mW. The

laser beam was directed towards the primary objective using a beam splitter which also allowed for white light images to be recorded of the sample surface. An electronic shutter was placed in the laser beam path in order to control patterning time. The laser beam was focused into a tight spot on the sample surface using a 50X Mitutoyo Plan Apo SL infinity corrected objective. Individual defects were patterned by exposing the sample surface to the laser beam for 1.3 - 1.5 seconds. The sample was then moved in the x-direction with the spacing between adjacent defects being around 2 μm. After a row had been written, the sample was displaced in the y-direction and another row of defects were then written. The overall patterning time to write a (22 x 18) μm² square lattice consisting of 120 defects was around 8 minutes.

The entire process, including stage and shutter control was automated using MATLAB, and allows any arbitrary pattern to be created (either periodic or aperiodic). Furthermore, the stages can also be used to write continuous lines along the X or Y direction. The laser patterning process can therefore in principle be used to write complex aperiodic potentials or other structures such as optical gratings.

Mirrors: DBR mirrors were deposited via electron-beam (e-beam) evaporation in an Angstrom Engineering deposition chamber at a base pressure of 4 x 10⁻⁶ mBar. The chamber contained two Telemark 25 cc e-beam sources equipped with high-strength graphite crucibles filled either with SiO_2 or Nb_2O_5. Silver mirrors were deposited by thermal evaporation using an Auto 306 Edwards thermal evaporator.

2D organic square lattices: The laser patterned PS layer was first coated with a 200 nm thick silver film. A DBR consisting of a pair of SiO_2 / Nb_2O_5 was then deposited onto the Ag surface, followed by a 400 nm thick layer of LFO / PS which was deposited by spin-coating. The cavity was then completed by depositing an additional 8 pairs of Nb_2O_5 / SiO_2 DBR by e-beam evaporation on the surface of LFO / PS, forming the top cavity mirror.

SURFACE CHARACTERIZATION

Scanning Force Microscopy: Surface topography images were acquired using an Asylum Research MFP-3D Bioscanning probe microscope. This was equipped with Bruker TESPA-V2 cantilevers with a force constant of 42 N / m and a resonance frequency of 320 kHz, with measurements made in tapping mode.

OPTICAL MEASUREMENTS

Basic optical characterization: All angle dependent PL, reflectivity and PL tomographic (real and Fourier-space) measurements were recorded using an Andor Shamrock SR-303i-A triple-grating imaging spectrograph having a focal length of 0.303 m. Measurements were made using a 300 groove / mm grating blazed at 500 nm except for k-space spectra measurements made on single defect or pairs of defects, in which a 1200 grooves / mm grating blazed at 500 nm was used. Angle dependent PL measurements using a goniometer were performed using a Thorlabs 405 nm diode laser. To generate PL tomographic scans, samples were excited using a pulsed, frequency doubled Ti:sapphire (coherent MIRA 900) laser at 445 nm, having a pulse width of ~ 150 fs, a nominal pulse repetition rate of ~ 76 MHz and an average power of ~ 5 μW. Reflectivity measurements were performed using a fiber coupled 20 W tungsten halogen light source (Ocean Optics DH-2000-BAL).

Goniometer setup: Angle-dependent reflectivity measurements were made using a goniometer setup consisting of two motorized arms fixed to a common rotation stage, where one arm was used for excitation while the other was used for collection. White light from the fiber coupled source was focused on to the sample using a pair of lenses and collected using a second pair of lenses, which was then fiber coupled to the spectrometer. The setup allowed reflectivity measurements to be made over an angular range of 10° to 70° in steps of 1°. A vertically displaced third arm was used for PL excita-

tion, in which the laser was focused on to the sample using a 100 mm focal length lens at an angle of incidence of ~ 15°. This configuration allowed PL to be collected over an angular range of 0° to 70°.

Fourier-space imaging and tomography setup: To extract k-space images of PL at $k_x = 0$, the laser was focused on the sample at normal incidence using an Edmund Optics 20X HR infinity corrected objective (numerical aperture (NA) = 0.60, focal length = 10 mm), with the PL collected via the same optical path using a beam splitter. Here a 200 mm lens was placed in the excitation path to create a spot size of ~ 16 μm (FWHM) on the sample surface. The collected PL was then focused into a spectrometer using a final 125 mm focal length collection lens, mounted on to an XYZ stage where the X-axis was motorized. An additional Fourier-plane imaging lens (focal length = 250 mm) was positioned before the final lens and allowed the Fourier-plane to be imaged by the spectrometer, with an effective demagnification of ~ 2. A dual-axis square slit was positioned at the focus of the imaging lens (before the final collection lens), which allowed the emission to be spatially filtered, permitting the unwanted real space signal to be rejected. In order to perform a tomographic scan, the motorized final collection lens was scanned across the spectrometer slits (k_x) and the intensity data from pixels along the CCD columns (k_y) was extracted, thereby permitting a map of the Fourier-space emission as a function of photon energy to be made.

Real-space imaging and tomography setup: To extract PL real-space images, the Fourier-space imaging setup described above was altered by introducing an additional lens (focal length = 25 mm) between the spatial filter and the final collection lens, thereby forming two telescopes with an effective magnification of 125X. The tomographic scan was again performed in a similar manner as described above, where the image across the spectrometer slit and the pixels along the CCD columns correspond to the x and y spatial-axes respectively.

Absorption measurements: Absorption measurements were performed using a Fluoromax 4 fluorometer (Horiba) equipped with a Xenon lamp.

OPTICAL MODELLING

Transfer matrix model: A transfer matrix model (which is described in detail in the 'Basics of optics multilayer systems'[45]) was used to simulate the angle-dependent reflectivity and PL emission from the planar microcavity structure. As input to the model, the absorption spectrum of the organic active layer was fitted using a series of Lorentzian functions, with the amplitude of the functions describing the excitonic oscillator strength.

Coupled oscillator model: The coupling between the cavity mode (E_{cav}) and the three organic transitions ($E_{org,n}$, where $n = 1$ to 3) of the LFO dye as a function of in-plane wave vector (k) can be described by the following Hamiltonian:

$$\begin{bmatrix} E_{cav}(k) - i\gamma_{cav} & g_1 & g_2 & g_3 \\ g_1 & E_{org,1}(k) - i\gamma_{org,1} & 0 & 0 \\ g_2 & 0 & E_{org,2}(k) - i\gamma_{org,2} & 0 \\ g_3 & 0 & 0 & E_{org,3}(k) - i\gamma_{org,3} \end{bmatrix}$$

where γ_{cav} and $\gamma_{org,n}$ correspond to the half-width half maximum (HWHM) of the cavity mode and the organic transitions respectively, and g_n is the coupling strength of the respective transitions with the cavity mode, where $n = 1$ to 3.

Band structure calculation: To calculate polariton lattices band structure we solve the time-independent Schrödinger equation, using an effective mass m_{LP} and in-plane potential $V(x, y)$. This al-

lows us to determine energy eigenvalues $E_n(k)$ where n is the band index and k is the polariton in-plane wave vector.

$$\left[-\frac{\hbar^2}{2m_{LP}}\nabla^2 + V(x,y)\right]\psi_{n,\boldsymbol{k}} = E_n(k)\psi_{n,\boldsymbol{k}}$$
(1)

Here, the photonic-nature of the polaritons allows us to use an approximated Hamiltonian, with a complete coupled exciton-photon Hamiltonian being unnecessary to reproduce the experimental observations [46,47]. The trapping potential of a single lattice site was assumed to take the form of a Gaussian $V(x,y) = -V_0 \exp\left(-\left(\frac{(x-x_0)^2}{2\sigma_x^2} + \frac{(y-y_0)^2}{2\sigma_y^2}\right)\right)$, where V_0 determines the potential trap depth, x_0 and y_0 give the centre coordinates and σ_x and σ_y are the trap-widths in the x and y directions. To construct a single unit cell, it was necessary to consider some overlap between the Gaussian tails of neighboring defects and thereby generate a smooth barrier at the interface between sites. This unit cell potential was implemented on a discretized 2D grid having sides of length a, with equation (1) being solved using a finite difference method with periodic boundary conditions along x and y, since $V(r) = V(r + a)$.

More insight into the experimental dispersion relations can be obtained by considering the expected emission intensity $I(n,k)$ of each calculated energy eigenstate. Since the measured PL signal derives from photons tunneling out of the cavity, we can estimate this intensity to be proportional to the overlapping probability density between each Bloch state $\psi_{n,\boldsymbol{k}}$ and a plane wave representing free-moving photons $\phi_{\boldsymbol{k}} = e^{i\boldsymbol{k}.\boldsymbol{r}}$, such that $I(n,k) \propto \left|\langle\phi_{\boldsymbol{k}}|\psi_{n,\boldsymbol{k}}\rangle\right|^2$ [48]. To reproduce the finite linewidth in energy (γ) and momentum (σ) of the measured emission, a Lorentzian term of the form $\frac{1}{(E-E_i)^2+\gamma^2}$ and Gaussian term of the form $\exp\left(-\frac{(k-k_i)^2}{\sigma^2}\right)$ were applied for each state (E_i, k_i) along the energy (E) and momentum (k) axes respectively[49].

ASSOCIATED CONTENT

Supporting Information (SI)

The Supporting Information (SI) is available free of charge on the ACS Publications website.

The SI (file type: .docx) contains the following information
1. Confinement in a deep defect
2. Depth and energy profile of the defects

AUTHOR INFORMATION

Corresponding Author

* e-mail: d.g.lidzey@sheffield.ac.uk

Present Addresses

† Ossila Ltd, Solpro Business Park, Windsor Street, Sheffield, S4 7WB, United Kingdom.

Author Contributions

D.G.L. initiated the study. The laser patterning setup was built by D.C. The initial patterning experiments were conducted by D.C. and R.J. Development of the experimental techniques and fabrication of structures was done by R.J. and K.G. with other measurements performed by O.G. and K.E.M. The band structure modelling calculations were performed by C.E.W. The manuscript was written by D.G.L., R.J. and C.E.W. with all authors providing comments. The authors declare that they have no conflict of interest.

Funding Sources

ABBREVIATIONS

PL, photoluminescence; 2D, two-dimenional; 1D, one-dimensional; DBR, distributed bragg reflectors; PS, polystyrene; SFM, scanning force microscopy; SLM, spatial sight modulator; LFO, lumogen F orange; TM, transfer matrix; LPB, lower polariton branch; UPB, upper polariton branch; e-beam, electron-beam; NA, numerical aperture; SI, supplementary information; FWHM, full width at half maximum.

REFERENCES

(1) Montambaux, G. Artificial Graphenes: Dirac Matter beyond Condensed Matter. *Comptes Rendus Phys.* **2018**, *19* (5), 285–305. https://doi.org/10.1016/j.crhy.2018.10.010.

(2) Leykam, D.; Flach, S. Perspective: Photonic Flatbands. *APL Photonics* **2018**, *3* (7), 70901. https://doi.org/10.1063/1.5034365.

(3) Khanikaev, A. B.; Shvets, G. Two-Dimensional Topological Photonics. *Nat. Photonics* **2017**, *11* (12), 763–773. https://doi.org/10.1038/s41566-017-0048-5.

(4) Hafezi, M.; Mittal, S.; Fan, J.; Migdall, A.; Taylor, J. M. Imaging Topological Edge States in Silicon Photonics. *Nat. Photonics* **2013**, *7*, 1001 EP-.

(5) Mittal, S.; Fan, J.; Faez, S.; Migdall, A.; Taylor, J. M.; Hafezi, M. Topologically Robust Transport of Photons in a Synthetic Gauge Field. *Phys. Rev. Lett.* **2014**, *113* (8), 87403. https://doi.org/10.1103/PhysRevLett.113.087403.

(6) Rechtsman, M. C.; Zeuner, J. M.; Tünnermann, A.; Nolte, S.; Segev, M.; Szameit, A. Strain-Induced Pseudomagnetic Field and Photonic Landau Levels in Dielectric Structures. *Nat. Photonics* **2012**, *7*, 153 EP-.

(7) Guzmán-Silva, D.; Mej\'\ia-Cortés, C.; Bandres, M. A.; Rechtsman, M. C.; Weimann, S.; Nolte, S.; Segev, M.; Szameit, A.; Vicencio, R. A. Experimental Observation of Bulk and Edge Transport in Photonic Lieb Lattices. *New J. Phys.* **2014**, *16* (6), 63061. https://doi.org/10.1088/1367-2630/16/6/063061.

(8) Bellec, M.; Kuhl, U.; Montambaux, G.; Mortessagne, F. Manipulation of Edge States in Microwave Artificial Graphene. *New J. Phys.* **2014**, *16* (11), 113023. https://doi.org/10.1088/1367-2630/16/11/113023.

(9) Poli, C.; Schomerus, H.; Bellec, M.; Kuhl, U.; Mortessagne, F. Partial Chiral Symmetry-Breaking as a Route to Spectrally Isolated Topological Defect States in Two-Dimensional Artificial Materials. *2D Mater.* **2017**, *4* (2), 25008. https://doi.org/10.1088/2053-1583/aa56de.

(10) Slobozhanyuk, A. P.; Khanikaev, A. B.; Filonov, D. S.; Smirnova, D. A.; Miroshnichenko, A. E.; Kivshar, Y. S. Experimental Demonstration of Topological Effects in Bianisotropic Metamaterials. *Sci. Rep.* **2016**, *6*, 22270 EP-.

(11) Kasprzak, J.; Richard, M.; Kundermann, S.; Baas, A.; Jeambrun, P.; Keeling, J. M. J.; Marchetti, F. M.; Szymańska, M. H.; André, R.; Staehli, J. L.; Savona, V.; Littlewood, P. B.; Deveaud, B.; Dang, L. S. Bose–Einstein Condensation of Exciton Polaritons. *Nature* **2006**, *443* (7110), 409–414. https://doi.org/10.1038/nature05131.

(12) Amo, A.; Lefrère, J.; Pigeon, S.; Adrados, C.; Ciuti, C.; Carusotto, I.; Houdré, R.; Giacobino, E.; Bramati, A. Superfluidity of Polaritons in Semiconductor Microcavities. *Nat. Phys.* **2009**, *5* (11), 805–810.

https://doi.org/10.1038/nphys1364.

(13) Amo, A.; Pigeon, S.; Sanvitto, D.; Sala, V. G.; Hivet, R.; Carusotto, I.; Pisanello, F.; Leménager, G.; Houdré, R.; Giacobino, E.; Ciuti, C.; Bramati, A. Polariton Superfluids Reveal Quantum Hydrodynamic Solitons. *Science (80-.).* **2011**, *332* (6034), 1167–1170. https://doi.org/10.1126/science.1202307.

(14) Sich, M.; Krizhanovskii, D. N.; Skolnick, M. S.; Gorbach, A. V; Hartley, R.; Skryabin, D. V; Cerda-Méndez, E. A.; Biermann, K.; Hey, R.; Santos, P. V. Observation of Bright Polariton Solitons in a Semiconductor Microcavity. *Nat. Photonics* **2011**, *6*, 50 EP-.

(15) Kartashov, Y. V; Skryabin, D. V. Two-Dimensional Topological Polariton Laser. *Phys. Rev. Lett.* **2019**, *122* (8), 83902. https://doi.org/10.1103/PhysRevLett.122.083902.

(16) Solnyshkov, D. D.; Bleu, O.; Malpuech, G. Topological Optical Isolator Based on Polariton Graphene. *Appl. Phys. Lett.* **2018**, *112* (3), 31106. https://doi.org/10.1063/1.5018902.

(17) Jacqmin, T.; Carusotto, I.; Sagnes, I.; Abbarchi, M.; Solnyshkov, D. D.; Malpuech, G.; Galopin, E.; Lema\^\itre, A.; Bloch, J.; Amo, A. Direct Observation of Dirac Cones and a Flatband in a Honeycomb Lattice for Polaritons. *Phys. Rev. Lett.* **2014**, *112* (11), 116402. https://doi.org/10.1103/PhysRevLett.112.116402.

(18) Whittaker, C. E.; Cancellieri, E.; Walker, P. M.; Gulevich, D. R.; Schomerus, H.; Vaitiekus, D.; Royall, B.; Whittaker, D. M.; Clarke, E.; Iorsh, I. V; Shelykh, I. A.; Skolnick, M. S.; Krizhanovskii, D. N. Exciton Polaritons in a Two-Dimensional Lieb Lattice with Spin-Orbit Coupling. *Phys. Rev. Lett.* **2018**, *120* (9), 97401. https://doi.org/10.1103/PhysRevLett.120.097401.

(19) Klembt, S.; Harder, T. H.; Egorov, O. A.; Winkler, K.; Ge, R.; Bandres, M. A.; Emmerling, M.; Worschech, L.; Liew, T. C. H.; Segev, M.; Schneider, C.; Höfling, S. Exciton-Polariton Topological Insulator. *Nature* **2018**, *562*, 552–556. https://doi.org/10.1038/s41586-018-0601-5.

(20) Nalitov, A. V.; Solnyshkov, D. D.; Malpuech, G. Polariton $\mathbb{Z}$ Topological Insulator. *Phys. Rev. Lett.* **2015**, *114* (11), 116401. https://doi.org/10.1103/PhysRevLett.114.116401.

(21) Amo, A.; Bloch, J. Exciton-Polaritons in Lattices: A Non-Linear Photonic Simulator. *Comptes Rendus Phys.* **2016**, *17* (8), 934–945. https://doi.org/https://doi.org/10.1016/j.crhy.2016.08.007.

(22) Schneider, C.; Winkler, K.; Fraser, M. D.; Kamp, M.; Yamamoto, Y.; Ostrovskaya, E. A.; Höfling, S. Exciton-Polariton Trapping and Potential Landscape Engineering. *Reports Prog. Phys.* **2017**, *80* (1), 016503. https://doi.org/10.1088/0034-4885/80/1/016503.

(23) Plumhof, J. D.; Stoeferle, T.; Mai, L.; Scherf, U.; Mahrt, R. F. Room-Temperature Bose-Einstein Condensation of Cavity Exciton-Polariton in a Polymer. *Nat. Mater.* **2014**, *13*, 247–252. https://doi.org/10.1038/nmat3925.

(24) Daskalakis, K. S.; Maier, S. a; Murray, R.; Kéna-Cohen, S. Nonlinear Interactions in an Organic Polariton Condensate. *Nat. Mater.* **2014**, *13* (3), 271–278. https://doi.org/10.1038/nmat3874.

(25) Cookson, T.; Georgiou, K.; Zasedatelev, A.; Grant, R. T.; Virgili, T.; Cavazzini, M.; Galeotti, F.; Clark, C.; Berloff, N. G.; Lidzey, D. G.; Lagoudakis, P. G. A Yellow Polariton Condensate in a Dye Filled Microcavity. *Adv. Opt. Mater.* **2017**, *5* (18), 1700203.

(26) Su, R.; Ghosh, S.; Wang, J.; Liu, S.; Diederichs, C.; Liew, T. C. H.; Xiong, Q. Observation of Exciton Polariton Condensation in a Perovskite Lattice at Room Temperature. *Nat. Phys.* **2020**, *16* (3), 301–306. https://doi.org/10.1038/s41567-019-0764-5.

(27) Dusel, M.; Betzold, S.; Egorov, O. A.; Klembt, S.; Ohmer, J.; Fischer, U.; Höfling, S.; Schneider, C. Room Temperature Organic Exciton–Polariton Condensate in a Lattice. *Nat. Commun.* **2020**, *11* (1), 2863. https://doi.org/10.1038/s41467-020-16656-0.

(28) Urbonas, D.; Stöferle, T.; Scafirimuto, F.; Scherf, U.; Mahrt, R. F. Zero-Dimensional Organic Exciton–Polaritons in Tunable Coupled Gaussian Defect Microcavities at Room Temperature. *ACS Photonics* **2016**, *3* (9), 1542–1545. https://doi.org/10.1021/acsphotonics.6b00334.

(29) Ramezani, M.; Halpin, A.; Fernández-Domínguez, A. I.; Feist, J.; Rodriguez, S. R.-K.; Garcia-Vidal, F. J.; Gómez Rivas, J. Plasmon-Exciton-Polariton Lasing. *Optica* **2017**, *4* (1), 31. https://doi.org/10.1364/OPTICA.4.000031.

(30) Hakala, T. K.; Moilanen, A. J.; Väkeväinen, A. I.; Guo, R.; Martikainen, J.-P.; Daskalakis, K. S.; Rekola, H. T.; Julku, A.; Törmä, P. Bose–Einstein Condensation in a Plasmonic Lattice. *Nat. Phys.* **2018**, *14* (7), 739–744. https://doi.org/10.1038/s41567-018-0109-9.

(31) Guo, L. J. Nanoimprint Lithography: Methods and Material Requirements. *Adv. Mater.* **2007**, *19* (4), 495–513. https://doi.org/10.1002/adma.200600882.

(32) Samuel, I. D. W.; Turnbull, G. A. Organic Semiconductor Lasers. *Chem. Rev.* **2007**, *107* (4), 1272–1295. https://doi.org/10.1021/cr050152i.

(33) Kappes, R. S.; Schönfeld, F.; Li, C.; Golriz, A. A.; Nagel, M.; Lippert, T.; Butt, H.-J.; Gutmann, J. S. A Study of Photothermal Laser Ablation of Various Polymers on Microsecond Time Scales. *Springerplus* **2014**, *3* (1), 489. https://doi.org/10.1186/2193-1801-3-489.

(34) Wang, B.; Wang, X. C.; Zheng, H. Y.; Lam, Y. C. Thermal Effect of Femtosecond Laser Polystyrene Processing. *Opt. Laser Technol.* **2019**, *117* (August 2018), 244–250. https://doi.org/10.1016/j.optlastec.2019.04.033.

(35) Wang, B.; Wang, X.; Zheng, H.; Lam, Y. C. Femtosecond Laser-Induced Nonlinear Absorption in Thick Polystyrene. *Lasers Manuf. Mater. Process.* **2019**, *6* (1), 59–66. https://doi.org/10.1007/s40516-019-0080-z.

(36) Naghilou, A.; Armbruster, O.; Kitzler, M.; Kautek, W. Merging Spot Size and Pulse Number Dependence of Femtosecond Laser Ablation Thresholds: Modeling and Demonstration with High Impact Polystyrene. *J. Phys. Chem. C* **2015**, *119* (40), 22992–22998. https://doi.org/10.1021/acs.jpcc.5b07109.

(37) Kim, B.-M.; Feit, M. D.; Rubenchik, A. M.; Joslin, E. J.; Eichler, J.; Stoller, P. C.; Da Silva, L. B. Effects of High Repetition Rate and Beam Size on Hard Tissue Damage Due to Subpicosecond Laser Pulses. *Appl. Phys. Lett.* **2000**, *76* (26), 4001–4003. https://doi.org/10.1063/1.126847.

(38) Dietrich, C. P.; Karl, M.; Ohmer, J.; Fischer, U.; Gather, M. C.; Höfling, S. Molding Photonic Boxes into Fluorescent Emitters by Direct Laser Writing. *Adv. Mater.* **2017**, *29* (16), 1605236. https://doi.org/10.1002/adma.201605236.

(39) Grant, R. T.; Michetti, P.; Musser, A. J.; Gregoire, P.; Virgili, T.; Vella, E.; Cavazzini, M.; Georgiou, K.; Galeotti, F.; Clark, C.; Clark, J.; Silva, C.; Lidzey, D. G. Efficient Radiative Pumping of Polaritons in a Strongly Coupled Microcavity by a Fluorescent Molecular Dye. *Adv. Opt. Mater.* **2016**, *4* (10), 1615–1623. https://doi.org/10.1002/adom.201600337.

(40) Winkler, K.; Fischer, J.; Schade, A.; Amthor, M.; Dall, R.; Geßler, J.; Emmerling, M.; Ostrovskaya, E. A.; Kamp, M.; Schneider, C.; Höfling, S. A Polariton Condensate in a Photonic Crystal Potential Landscape. *New J. Phys.* **2015**, *17* (2), 023001. https://doi.org/10.1088/1367-2630/17/2/023001.

(41) Amo, A.; Bloch, J. Exciton-Polaritons in Lattices: A Non-Linear Photonic Simulator. *Comptes Rendus Phys.* **2016**, *17* (8), 934–945. https://doi.org/10.1016/j.crhy.2016.08.007.

(42) Lidzey, D. G.; Bradley, D. D. C.; Armitage, A.; Walker, S.; Skolnick, M. S. Photon-Mediated Hybridization of Frenkel Excitons in Organic Semiconductor Microcavities. *Science* **2000**, *288* (5471), 1620–1623. https://doi.org/10.1126/science.288.5471.1620.

(43) Coles, D. M.; Somaschi, N.; Michetti, P.; Clark, C.; Lagoudakis, P. G.; Savvidis, P. G.; Lidzey, D. G. Polariton-Mediated Energy Transfer between Organic Dyes in a Strongly Coupled Optical Microcavity. *Nat. Mater.* **2014**, *13* (7), 712–719. https://doi.org/10.1038/nmat3950.

(44) Georgiou, K.; Michetti, P.; Gai, L.; Cavazzini, M.; Shen, Z.; Lidzey, D. G. Control over Energy Transfer between Fluorescent BODIPY Dyes in a Strongly-Coupled Microcavity. *ACS Photonics* **2018**, *5* (1), 258–266. https://doi.org/10.1021/acsphotonics.7b01002.

(45) Furman, S. A.; Tikhonravov, A. V. Spectral Characteristics of Multi-Layer Coatings: Theory. In *Basics of optics of multilayer systems*; Atlantica Séguier Frontières: Paris, 1992; Vol. 0, pp 1–102.

(46) Kim, N. Y.; Kusudo, K.; Wu, C.; Masumoto, N.; Löffler, A.; Höfling, S.; Kumada, N.; Worschech, L.; Forchel, A.; Yamamoto, Y. Dynamical D-Wave Condensation of Exciton–Polaritons in a Two-Dimensional Square-Lattice Potential. *Nat. Phys.* **2011**, *7* (9), 681–686. https://doi.org/10.1038/nphys2012.

(47) Kim, N. Y.; Kusudo, K.; Löffler, A.; Höfling, S.; Forchel, A.; Yamamoto, Y. Exciton{\textendash}polariton Condensates near the Dirac Point in a Triangular Lattice. *New J. Phys.* **2013**, *15* (3), 35032. https://doi.org/10.1088/1367-2630/15/3/035032.

(48) Lai, C. W.; Kim, N. Y.; Utsunomiya, S.; Roumpos, G.; Deng, H.; Fraser, M. D.; Byrnes, T.; Recher, P.; Kumada, N.; Fujisawa, T.; Yamamoto, Y. Coherent Zero-State and π-State in an Exciton–Polariton Condensate Array. *Nature* **2007**, *450* (7169), 529–532. https://doi.org/10.1038/nature06334.

(49) Pan, H.; Winkler, K.; Powlowski, M.; Xie, M.; Schade, A.; Emmerling, M.; Kamp, M.; Klembt, S.; Schneider, C.; Byrnes, T.; Höfling, S.; Kim, N. Y. Two-Kind Boson Mixture Honeycomb Hamiltonian of Bloch Exciton-Polaritons. *Phys. Rev. B* **2019**, *99* (4), 45302. https://doi.org/10.1103/PhysRevB.99.045302.